Article:
Turner, S, Williams, H, Piazolo, S et al. (2018) Sub-arc xenolith Fe-Li-Pb isotopes and textures tell tales of their journey through the mantle wedge and crust. Geology, 46 (11). pp. 947-950. ISSN: 0091-7613

https://doi.org/10.1130/G45359.1

Sub-arc xenolith Fe-Li-Pb isotopes and textures tell tales of their journey through the mantle wedge and crust

Simon Turner[1], Helen Williams[2], Sandra Piazolo[1,†], Janne Blichert-Toft[3], Mitchel Gerdes[1], John Adam[1], Xiao-Ming Liu[4], Bruce Schaefer[1] and Rene Maury[5]

[1]Department of Earth and Planetary Sciences, Macquarie University, Sydney 2109, Australia
[2]Department of Earth Sciences, University of Cambridge, Cambridge CB2 3EQ, UK
[3]Laboratorie de Géologie de Lyon, Ecole Normale Supérieure de Lyon, Université Claude Bernard Lyon 1, CNRS UMR 5276, 46 Allée d'Italie, 69007 Lyon, France
[4]Department of Geological Sciences, University of North Carolina, Chapel Hill, NC, 27599, USA
[5]UMR CNRS 6538 Domaines Océaniques, Universite de Bretagne Occidentale, BP 809, 29285 Brest, France

E-mails: simon.turner@mq.edu.au; hmw20@cam.ac.uk; jblicher@ens-lyon.fr; s.piazolo@leeds.ac.uk; mitchell.gerdes@hdr.mq.edu.au; john.adam1@bigpond.com; xiaomliu@email.unc.edu; bruce.schaefer@mq.edu.au; rene.maury@univ-brest.fr

[†]Now at: School of Earth and Environment, University of Leeds, Leeds, LS2 9JT, UK

ABSTRACT

Island arcs provide insights into the origin and recycling of continental crust. However, questions remain concerning source metasomatism, the depth of differentiation, the potential role of amphibole fractionation and the timescales involved. One problem is that our knowledge is largely restricted to inferences from erupted lava compositions. Rare, compound xenoliths, described here, provide a complementary perspective. Basaltic andesites on Batan Island (the Philippines), contain ≥ 150 Ma peridotite fragments encased in hornblendite and gabbroic rinds. The peridotites have some of the lightest δ^{7}Li and δ^{57}Fe values yet measured in mantle rocks. They appear to have captured the effects of melt depletion combined with slab fluid addition and potentially be derived from diffusion-modified melt channel wall-rocks. Stable isotope signals are easily modified by diffusive equilibration between peridotite and host magma so the preservation of light δ^{7}Li and δ^{57}Fe here suggests magma ascent rates of ~ 10 km yr^{-1}. Melt – wall-rock reactions at ~ 25-30 km depth led to the crystallisation of amphibole (± plagioclase) and fractionation from basalt to basaltic andesite. This provides a location and mechanism for the "cryptic" amphibole fractionation observed in these and perhaps many other arc lavas and may obviate the need for delamination of cumulates. Subsequently, the basaltic andesite underwent gabbroic fractionation at ~ 7 km depth prior to final eruption.

INTRODUCTION

Arc lavas and the generation of continental crust are the end products of a complex, multi-stage process that begins with addition of slab-derived components to the mantle wedge followed by partial melting and melt ascent. Few erupted arc magmas are primary, complicating inferences about mantle wedge processes and raising important questions concerning differentiation. For example, it is debated whether differentiation occurs at depth near the Moho (Annen et al., 2006), followed by delamination of dense cumulates (Jull and Kelemen, 2001), or far more shallowly (Adam et al., 2016). The extent to which differentiation involves "cryptic" amphibole fractionation (Davidson et al., 2007) is also debated and there is a lack of concensus about the mechanism and location involved. Similarly, the relative contribution of components from the altered oceanic crust and/or overlying sediments, whether these are transferred as fluids or melts, and the mechanism of melt ascent, all remain controversial (Plank, 2005; Spandler and Pirard, 2013.). These ongoing debates require a complementary approach that we argue here can be provided by the study of rare, sub-arc mantle xenoliths.

SAMPLES AND DATA

Our samples are amphibole-bearing, clinopyroxene-poor peridotite xenoliths entrained in basaltic-andesite pyroclastics and lavas erupted 1480 yr BP from Mount Iraya volcano on Batan Island in the Philippines (Maury et al., 1992; Arai et al., 2004). A typical xenolith consists of peridotite fragments encased by a hornblendite that is surrounded by a hornblende gabbro and finally the basaltic andesite that brought the composite to the surface. Here we report bulk rock Li-Fe stable and radiogenic Pb isotope data for six peridotites, a representative host lava and the local subducting sediment (Table DR1 in the GSA Data Repository). B isotopes for the host lava and sediment are also given in Table DR1. Major and trace elements along with Sr, Nd and U-Th-Ra isotope data for the same peridotites and host lava were presented by Turner et al. (2012). Mineral chemistry is provided in Tables DR2 and 3 and in Turner et al. (2012). Re-Os isotope data for

olivine from one of the peridotites is given in Table DR4.

ISOTOPIC INSIGHTS INTO MANTLE WEDGE PROCESSES

Olivine grains from the core of one of the peridotites preserve a rhenium depletion model age (T_{RD}) of 147 Ma (Table DR4). Given that this is, by definition, a minimum age and it implies the peridotite experienced significant melt depletion at, or prior to, this time and well before the initiation of subduction in the Philippines. They may derive from an ancient asthenospheric domain in the mantle wedge, like those sampled beneath some spreading centres (e.g. Harvey et al., 2006).

Strikingly, our data from Batan include some of the lightest Li and Fe isotope ratios yet reported for mantle peridotites, in stark contrast to those reported for the sub-arc xenolith suite from Avacha, Kamchatka (Pogge von Strandmann et al., 2011; Weyer and Ionov, 2007). Nevertheless, light Li and Fe isotopes have been observed previously in peridotites, eclogites, serpentinites and olivine veins (e.g. Debret et al., 2016; Penniston-Dorland et al., 2010; Weyer and Ionov, 2007).

It is well established that the Batan peridotites have incompatible trace element and isotope relationships resembling those of their host lavas (Maury et al., 1992; Turner et al., 2012) and these can be explained by a 3-component mixture comprising mantle wedge, sediment and slab-fluid components (Turner et al., 2012). The host lava has rather low $\delta^{11}B$ (-5.6) and $\delta^{7}Li$ (2.0) values that are consistent with addition of sediment to the mantle wedge. As shown in Fig. 1A, the peridotites form a steep array that extends from a $\delta^{7}Li$ value resembling their host lava towards a very low $\delta^{7}Li$ of -1.8 ‰ and this is accompanied by increasing $^{206}Pb/^{204}Pb$. Back-projection of this array intersects a mixing curve between the composition inferred for the mantle wedge and the local sediment (~ 0.07% required). A similar relationship is observed between $\delta^{7}Li$ and $^{87}Sr/^{86}Sr$ (not shown) though relationships with $^{208}Pb/^{204}Pb$, $^{207}Pb/^{204}Pb$ and $^{143}Nd/^{144}Nd$ are less informative.

Slab-fluid addition could explain the trend of the peridotites towards light $\delta^{7}Li$, either because the slab undergoes progressive fluid loss of heavy $\delta^{7}Li$ value leading to increasingly light $\delta^{7}Li$ in subsequent fluids (e.g., Zack et al., 2003), and/or because later fluid release comes from

deeper in the slab where δ^7Li is known to be the lightest (Gao et al., 2012). However, the Batan peridotites show a far greater range in δ^7Li than most arc lavas (δ^7Li = 1-5 ‰, Elliott et al., 2004) many of which may have undergone diffusive equilibration with the ambient wedge.

In Fig. 1B, peridotite δ^{57}Fe decreases from typical mantle melt value of 0.11 ± 0.04 ‰, as observed for the host lava, to -0.46 ± 0.06 ‰ significantly lower than the lowest δ^{57}Fe yet measured in arc lavas (grey bar on Fig. 1B). Three different mechanisms have been proposed to explain how light Fe isotopes can develop in peridotite: (1) melt extraction whereby the heavy ^{57}Fe isotope is preferentially removed (e.g., Williams and Bizimis, 2014), most likely under conditions that are redox-buffered by addition of fluids from the slab (Foden et al., 2018); (2) addition of slab-fluids that have light δ^{57}Fe (see discussions by Nebel et al., 2015 and Foden et al., 2018); (3) diffusive extraction of ^{57}Fe by repeated interaction with rapidly passing of melts that leads to melt channel wall-rocks comprised of olivine with light δ^{57}Fe (Weyer and Ionov, 2007; Foden et al., 2018).

Distinguishing between these scenarios is difficult and the extreme Li and Fe isotope ratios observed seem to require positive reinforcement of all three. In our preferred model, the peridotite fragments record the addition of slab fluids to deforming mantle that had earlier undergone variable melt depletion. Given the clinopyroxene-poor nature of the Batan peridotites (cf. Maury et al., 1992; Arai et al., 2004), melt depletion must have played a significant role in generating their low δ^{57}Fe values. However, poor correlations between δ^{57}Fe and Al or Cr# (not shown) do not support this being the sole mechanism at work. Nebel et al. (2015) have shown that acceptable amounts of sediment or mélange addition (cf. Fig. 1A) are incapable of changing Fe isotopes in arc magma source regions and this holds true for the Batan xenoliths given the relatively high δ^{57}Fe of the Philippine sediment (Fig. 1B). Instead, the decrease in δ^{57}Fe is accompanied by increasing U/Th (Fig. 1B) suggesting some of the shift to light Fe isotope values achieved through prior melt depletion must have been augmented by addition of slab fluids (Nebel et al., 2015; Foden et al., 2018). We also observe that δ^7Li and δ^{57}Fe co-vary with ^{206}Pb/^{204}Pb and U/Th. Increases in U/Th ratios in arc lavas (that range from 0.2 to > 1) can result from both prior melt depletion of the

mantle wedge and slab-fluid addition. Debret et al. (2016) have recently documented low-δ^{57}Fe fluids derived from slab-sulfide breakdown in serpentinites from the western Alps and high sulfur contents characterize the Batan peridotites (Metrich et al., 1999). Caveats to this being the sole process are the high fluid/rock ratios required and that slab-fluid Fe contents are likely too low to perturb mantle wedge δ^{57}Fe more than 0.1 ‰ (see Fig. DR2 and disucssion). Thus, we speculate that the peridotite fragments come from the wall rocks of melt channels where further lowering of δ^{57}Fe occured by repeated interaction with rapidly passing of melts as discussed by Foden et al. (2018). On Fig. 1B we show three schematic arrows that indicate the relative shift in δ^{57}Fe that could be produced by buffered fractional melting (from Foden et al., 2018) and slab fluid addition (from Nebel et al., 2015). The grey arrow illustrates the remaining decrease in δ^{57}Fe required by repeated melt passage.

We cannot rule out the possibility that these processes may have been augmented by the effects of diffusion between peridotite and host magma as discussed by Pogge von Strandmann et al. (2011). However, it is not clear what the driving mechanism for Fe isotope diffusion would be, given the near-identical FeO contents of the peridotites and host magma (Table DR1). Either way, the lack of good correlation between δ^{7}Li and 1/Li, or δ^{57}Fe and 1/FeO*, or between δ^{7}Li and δ^{57}Fe (Figs. DR1 and 2) indicates that diffusion was not the sole process. Instead, the Batan peridotites appear to have "captured" a snapshot of processes that, in the case of most arc rocks such as the host lava analysed here, are often overprinted by diffusion with the ambient wedge s(Weyer and Ionov, 2007; Elliott et al., 2004). Importantly, the preservation of these signatures requires transport to the surface within years to decades (e.g. Pogge von Strandmann et al., 2011) and the rapid (days to months) rate of dissolution of mantle xenoliths in basaltic magma may demand even faster transit times (Brearley and Scarfe, 1986).

INSIGHTS INTO CRUSTAL PROCESSES FROM TEXTURES AND HOST LAVAS

Striking new insights also come from the textures of the coarse-grained, angular peridotite

154 fragments (Mg# = 88-91) and the one from which our petrological data were obtained is shown in
155 Fig. 2. This which is an example of the coarse-grained or "C-type xenoliths" of Arai et al. (2004)
156 and is encased within hornblendite (~ 100% pargasite) and subsequently hornblende gabbro (50%
157 pargasite, 50% anorthite). The peridotite fragments from this xenolith are comprised of around 78%
158 olivine (Fo_{91-78}), > 9% orthopyroxene ($En_{82}Fs_{17}Wo_{1}$), < 7% clinopyroxene ($En_{49}Fs_{8}Wo_{43}$) and ~ 6%
159 chromian spinel (Cr# 0.3-0.6). Thermometry indicates their last equilibration at a temperature of
160 920 ºC (Gerdes, 2016) although some Batan peridotites record hotter temperatures (up to 1100 ºC)
161 and probably originated from greater depths (Arai et al., 2004).
162 Quantitative orientation analysis showing systematic crystal lattice bending and sub-grain
163 boundaries (Figs. 2E, F) suggests that the peridotite was subject to crystal plastic deformation
164 before the hornblende-rich shells formed. Therefore it is not a cumulate, consistent with the
165 presence of chromian spinel and textural evidence that the transition from C- to F-type (fine-
166 grained) peridotites resulted from shearing and metasomatism during induced convection in the
167 mantle wedge (Arai et al., 2004). The fact that the peridotite fragments are never found in direct
168 contact with the hornblende-gabbro (Fig. 2C) suggests formation of the latter by reaction of the
169 peridotite with melt. Mineral chemistry (Tables DR2 and 3) from the hornblendite and hornblende
170 gabbro that surround the peridotite fragments in Fig. 2 indicate temperatures of ~ 1000 ºC (Gerdes,
171 2016). The presence of spinel, but absence of plagioclase in equilibrium with the olivine, indicates
172 pressures of 0.7-0.8 GPa, based on the spinel- to plagioclase-lherzolite transition (Borghini et al.,
173 2010). Thus, these reaction shells formed at ~ 25-30 km depth, significantly deeper than the last
174 equilibration point of their host lava (~ 7 km) as discussed below.
175 The textural make-up of the xenoliths can be explained by hydrous basaltic melt ascending
176 through channels in a deformed sub-arc mantle wedge causing both fragmentation through
177 hydrofracturing (e.g. Tretiakova et al., 2017) and melt-rock interactions of the following general
178 type:

179 hydrous basaltic melt + olivine ⇒ amphibole ± clinopyroxene (1)

hydrous basaltic melt ⇒ amphibole + plagioclase (2)

where reaction (1) forms the hornblendite with minor clinopyroxene (Fig. 2) and reaction (2) forms the hornblende gabbro. The key significance of the dual process of fracturing and melt-rock reaction is that the newly fractured peridotite represents a highly reactive surface both physically and chemically triggering local amphibole growth at the fragment-melt interfaces. Disequilibrium between the magma and the peridotite induces local dissolution of olivine (i.e. grain scale magmatic assimilation of olivine) and crystallisation of hornblende from the fluxing magma at the reaction front. Texturally, this process is supported by the remnants of olivine grains of the same crystallographic orientation (Fig. 2E), hence belonging to the same original grain, within newly grown hornblende. Furthermore, entrainment of and reaction with the peridotite is well documented by "veinlets" of hornblende and clinopyroxene within the peridotite fragments (Figs. 2D, F).

The basaltic andesite has 52 wt. % SiO_2 and an anhydrous mineral assemblage consisting of 36% plagioclase (An_{87-71}), 13% clinopyroxene ($En_{48}Fs_{14}Wo_{38}$), 1% orthopyroxene ($En_{70}Fs_{28}Wo_2$) and 1% magnetite contained in a microcrystalline groundmass (49%). It last equilibrated at 1080 ºC at a pressure of 0.3 GPa (Gerdes, 2016). Like most arc lavas, this suggests temporary residence at ~ 7 km depth within the crust (Adam et al., 2016) where it would have been water saturated with ≥ 4 wt. % H_2O (Stern et al., 1975). Melt inclusions within olivines in some of these peridotites have H_2O contents of 4.4-5.2 wt. % (Schiano et al., 1995).

It is significant that the phenocryst assemblage of the host lava has a bulk SiO_2 content of ~ 50 wt. % and so does not have sufficient leverage to be responsible for the differentiation of the basaltic andesite from a basaltic parent (although fractionation of this assemblage can yield the andesitic composition of the groundmass (58 wt. % SiO_2) from a basaltic andesite precursor). Rather, there is a negative relationship between Dy/Yb and SiO_2 amongst the Mount Iraya lavas (Fig. 3) that is typical of many arc lavas and which Davidson et al. (2007) used to infer amphibole fractionation (note there is no correlation between Dy/Yb and radiogenic isotopes in these lavas). Although a combination of olivne + clinopyroxene + plagioclase (i.e. located within the dotted

206 triangle on Fig. 3) could lead to a similar result, this assemblage is not observed in cumulates found
207 at Iraya and is likely to be more important in high-temperature, low-alkali systems where amphibole
208 becomes increasingly unstable. Instead, the process of reaction-replacement (Smith, 2014; Daczko
209 et al., 2016) provides a new mechanism for "cryptic" amphibole fractionation. Our barometry
210 indicates that this occurred at ~ 25-30 km depth and so well below the Moho which lies at ~15 km
211 beneath Batan Island (Dimalanta and Yumul, 2003).
212
213 **SUMMARY FROM BOTTOM TO TOP**
214 To the best of our knowledge our study is one of the first to directly document the bottom-
215 to-top history in an arc magmatic system. The peridotite fragments once existed in some part of the
216 actively deforming, metasomatised mantle wedge and, as such, represent unique analogues of the
217 arc source (Maury et al., 1992; Turner et al., 2012). Their composition records ancient (but
218 probably semi-continuous) melt depletion then pervasive metasomatism by slab-derived fluids that
219 were added only 100-1000 yrs prior to eruption (Turner et al., 2012). We suggest that they represent
220 pieces of melt channel wall rocks from which heavy $\delta^{57}Fe$ was extracted by transiting melts.
221 Subsequent amphibole-forming reactions with ascending hydrous melts provide a mechanism for
222 "cryptic" amphibole fractionation and it appears that this occurred well below the Moho. The
223 implication is that many magmas crossing this boundary may have already differentiated beyond
224 basaltic compositions with the corollary that the mass balance arguments used to argue for the need
225 to delaminate large volumes of cumulates beneath arcs (Jull and Kelemen, 2001) can be relaxed.
226 Further fractionation to more evolved compositions (andesitic groundmass) occurred at shallow
227 depths in the arc crust as shown by Adam et al. (2016). The final ascent of the composite xenoliths
228 arguably occurred within months or less and the fast timescales inferred throughout preclude
229 models invoking diapiric rise that have become so popular in the recent literature. Whether these
230 conclusions apply only locally or equally to other arcs remain to be established.
231

Acknowledgements

We thank Sonia Tonorini for the B isotope analyses and Gerhard Wörner, Roberta Rudnick, and Nathan Daczko for comments. The manuscript was prepared whilst S.T. was Gauss Professor at the University of Göttingen courtesy of the Akademie der Wissenschaften zu Göttingen. H.W. acknowledges help in mass spectrometry by Geoff Nowell and funding from the ERC (Starting Grant "HabitablePlanet", 306655) and NERC ("Deep Volatiles", NE/M0003/1). Xiao-Ming Liu was supported by NSF grant EAR0948549 to Roberta Rudnick and Bill McDonough. We dedicate this work to the memory of the late Jon Davidson whose humility, enthusiasm and friendship inspired so many and is sadly missed. The editorial assistance of Chris Clark and reviews by M. Gregoire, Paolo Sossi and an anonymous reviewer helped improve the final manuscript.

243 **REFERENCES CITED**

244 Adam, J., Turner, S., and Rushmer, T., 2016, The genesis of silicic magmas in shallow crustal cold
245 zones: Lithos, v. 264, p. 472–494.
246 Annen, C., Blundy, J.D., and Sparks, R.S.J., 2006, The genesis of intermediate and silicic magmas
247 in deep crustal hot zones: Journal of Petrology, v. 47, p. 505–540.
248 Arai, S., Takada, S., Ashi, K.M., and Kida, M., 2004, Petrology of peridotite xenoliths from Iraya
249 volcano, Philippines, and its implication for dynamic mantle-wedge processes: Journal of
250 Petrology, 45, p. 369-389.
251 Borghini, G., Fumagalli, P., and Rampone, E., 2010, The stability of plagioclase in the upper
252 mantle: subsolidus experiments on fertile and depleted lherzolite: Journal of Petrology, 51, p.
253 229-254.
254 Brearley, M., and Scarfe, C.M., 1986, Dissolution rates of upper mantle minerals in an alkali basalt
255 melt at high pressure: an experimental study and implications for ultramafic xenolith survival:
256 Journal of Petrology, v. 27, p. 1157-1182.
257 Daczko, N.R., Piazolo, S., Meek. U., Stuart, C.A., and Elliott, V., 2016, Hornblendite delineates
258 zones of mass transfer through the lower crust: Scientific Reports, v. 6, doi:
259 10.1038/srep31369.
260 Davidson, J., Turner, S., Dosseto, A., and Handley, H., 2007. Amphibole “sponge” in arc crust?
261 Geology, v. 35, p. 787–790.
262 Debret, B., Millet, M.-A., Pons, M.-L., Bouihol, P., Inglis, E., and Williams, H., 2016, Isotopic
263 evidence for iron mobility during subduction: Geology, v. 44, p. 215-218.
264 Dimalanta, C.B., and Yumul, G.P., 2003, Magmatic and amagmatic contributions to crustal growth
265 of an island-arc system: the Philippine example: International Geology Review, v. 45, p. 922-
266 935.
267 Elliott, T., Jeffcoate, A., and Bouman, C., 2004, The terrestrial Li isotope cycle: light-weight
268 constraints on mantle convection: Earth and Planetary Science Letters, v. 220, 231–245.
269 Foden, J., Sossi, P.A., and Nebel, O, 2018, Controls on the iron isotopic composition of global arc
270 magmas: Earth and Planetary Science Letters, v. 494, p. 190-201.
271 Gao, Y., Vils, F., Cooper, K.M., Banerjee, N., Harris, M., Hoefs, J., Teagle, D.A.H., Casey, J.F.,
272 Elliott, T., Laverne, C., Alt, J.C., and Muechlenbachs, 2012, Downhole variation of lithium
273 and oxygen isotopic compositions of oceanic crust at East Pacific Rise, ODP Site 1256:
274 Geochimica et Cosmochimica Acta, v. 13, Q10001.
275 Gerdes, M., 2016, Amphibole and magma evolution – Batan Island, Philippines: MSc, Macquarie
276 University, pp. 58.
277 Harvey, J., Gannoun, A ., Burton, K.W., Rogers, N.W., Alard, O., and Parkinson, I.J.,2006, Ancient

melt extraction from the oceanic upper mantle revealed by Re-Os isotopes in abyssal peridotites from the Mid-Atlantic ridge: Earth and Planetary Science Letters, v. 244, p. 606-621.

Jull, M., and Kelemen, P., 2001. On the conditions for lower crustal convective instability: Journal of Geophysical Research, V. 106, p. 6423-6446.

Leeman, W.P., Tonarini, S., and Turner, S., 2017, Boron isotope variations in Tonga-Kermadec-New Zealand arc lavas: implications for origin of subduction components and mantle influences: Geochemistry, Geophysics Geosystems v. 18, doi:10.1002/2016GC006523.

Maury, R.C., Defant, M.J., and Joron, J.L., 1992, Metasomatism of the sub-arc mantle inferred from trace elements in Philippine xenoliths: Nature, v. 360, p. 661–663.

Metrich, N., Schiano, P., Clocchiatti, R., and Maury, R.C., 1999, Transfer of sulfur in subduction settings: an example from Batan Island (Luzon volcanic arc, Philippines): Earth and Planetary Science Letters, v. 167, p. 1-14.

Nebel, O., Sossi, P.A., Benard, A., Wille, M., Vroon, P.Z., and Arculus, R.J., 2015, Redox-variability and controls in subduction zones from an iron-isotope perspective: Earth and Planetary Science Letters, v.432, p. 142-151.

Penniston-Dorland, S.C., Sorenson, S.S., Ash, R.D., and Khadke, S.V., 2010, Lithium isotopes as a tracer of fluids in a subduction zone mélange: Franciscan Complex, CA: Earth and Planetary Science Letters, v. 292, p. 181-190.

Plank, T., 2005, Constraints from Thorium/Lanthanum on sediment recycling at subduction zones and the evolution of the continents: Journal of Petrology v. 46, p. 921–944.

Pogge von Standmann, P.A.E., Elliott, T., Marshcall, H.R., Coath, C., Lai, Y.-J., Jeffcoate, A.B., and Ionov, D.A., 2011, Variations of Li and Mg isotope ratios in bulk chondrites and mantle xenoliths: Geochimica et Cosmochimica Acta, v. 75, p. 5247-5268.

Sajona, F.G., Maury, R.C., Prouteau, G., Cotton, J., Schiano, P., Bellon, H., and Fontaine, L., 2000, Slab melt as metasomatic agent in island arc mantle sources, Negros and Batan (Philippines): Island Arc, v. 9, p. 472-486.

Schiano, P., Clocchiatti, R., Shimizu, N., Maury, R.C., Jochum, K.P., and Hofmann, A.W., 1995, Hydrous, silica-rich melts in the sub-arc mantle and their relationships with erupted arc lavas: Nature, v. 377, p. 595-600.

Smith, D.J., 2014, Clinopyroxene precursers to amphibole sponge in the arc crust: Nature Communications, v. **5**, 4329.

Spandler, C., and Pirard, C., 2013, Element recycling from subducting slabs to crust: A review: Lithos, v. 170– 171, p. 208–223.

Stern, C.R., Huang, W.-L., and Wyllie, P.J., 1975, Basalt0andesite-rhyolite-H_2O: Crystallization

intervals with excess H_2O and H_2O-undersaturated liquidus surfaces to 35 kilobars, with implications for magma genesis: Earth and Planetary Science Letters, v. 28, p. 189-196.

Tretiakova, I.G., Belousova, E.A., Malkovets, V.G., Griffin, W.L., Piazolo, S., Pearson, N.J., O'Reilly, S.Y., and Nishido, H., 2017, Recurrent magmatic activity on a lithosphere-scale structure: Crystallization and deformation in kimberlitic zircons: Gondwana Research, v. 42, p.126-132.

Turner, S., Caulfield, J., Turner, M., van Keken, P., Maury, R., Sandiford, M., and Prouteau, G., 2012, Recent contribution of sediments and fluids to the mantle's volatile budget: Nature Geoscience, v. 5, p. 50–54.

Weyer, S., and Ioniv, D.A., 2007, Partial melting and melt percolation in the mantle: the message from Fe isotopes: Earth and Planetary Science Letters, v. 259, p. 119-133.

Williams, H., and Bizimis, M., 2014, Iron isotope tracing of mantle heterogeneity within the source regions of oceanic basalts: Earth and Planetary Science Letters, v. 404, p. 396–407.

Zack, T., Tomascak, P., Rudnick, R.L., Dalpe, C., and McDonough, W.F., 2003, Extremely light Li in orogenic eclogites: the role of isotope fractionation during dehydration in subducted oceanic crust: Earth and Planetary Science Letters, v. 208, p. 270-290.

Figure 1. Stable isotope systematics in Batan xenoliths. A: Plot of δ^7Li versus ^{206}Pb/^{204}Pb showing mixing curve between a depleted MORB mantle source (DMM) and locally subducting terrigenous sediment (mixing parameters in Table DR1). The xenoliths depart from this curve towards an inferred fluid component having very low δ^7Li. B: Negative trend between δ^{57}Fe and U/Th indicating that the most depleted peridotites (as recorded by low δ^{57}Fe) are most strongly affected by fluid addition leading to higher U/Th ratios. Range of δ^{57}Fe in arc lavas in (B) is from Foden et al. (2018). The relative size of the buffered melt depletion vector of from Foden et al. (2018), fluid addition (water/rock ratio = 4:1) from Nebel et al. (2015) and unconstrained for melt channel pre-conditioning. See text for discussion.

Figure 2. Composite xenolith from Batan Island. A: Photos showing peridotite encased in hornblendite and subsequently a hornblende gabbro and finally the basaltic andesite that brought them to the surface. B: Section through xenoliths clearly showing the angular peridotite fragments encased in hornblendite and hornblende gabbro. C: Example of neutron beam image showing that throughout the xenoliths peridotite fragments are always surrounded by hornblendite. D: (left) Photomicrograph of contact between hornblendite and peridotite fragment (right) close-up maps showing distribution of phases (white shows unindexed areas); top and bottom map corresponds to maps shown in E and F, respectively. E: Close-up of reaction front between hornblende shell and peridotite showing that olivine has subgrain boundaries, while hornblende has not; note also that hornblende "fingers" into olivine along sub-grain boundaries. Some unreacted olivine remnants are observed within the hornblende grain; insets show 3D orientation of grains, colour scheme shows different crystallographic orientations in different colours, for boundary colour scheme see legend. F: Reactive "veinlets" invading the olivine; note that newly grown hornblende and clinopyroxne grains are intergrown while olivine remnants are apparent, colour scheme shows different crystallographic orientations in different colours; for boundary colour scheme see legend.

Note D-F are results from Electron Backscatter Diffraction Analysis; scale bars are 200 μm.

Figure 3. Dy/Yb versus SiO_2 in minerals and host lavas. The geometric relationships between the minerals from the xenoliths and the lavas from Mount Iraya (data from Sajona et al., 2000) are interpreted as crystallisation of amphibole (i.e., the hornblendite) that can account for the compositional variation in the host lavas whereas the primary phenocryst assemblage in either the peridotites or the host lavas cannot (amount of amphibole crystallization is indicated in %). Dashed triangle illustrates a possible residual mineral combination (not observed in Iraya cumulates) that could have the same effect. Mineral trace element data from Table DR2 and Turner et al. (2012), bulk peridotite data from Turner et al. (2012). See text for discussion.

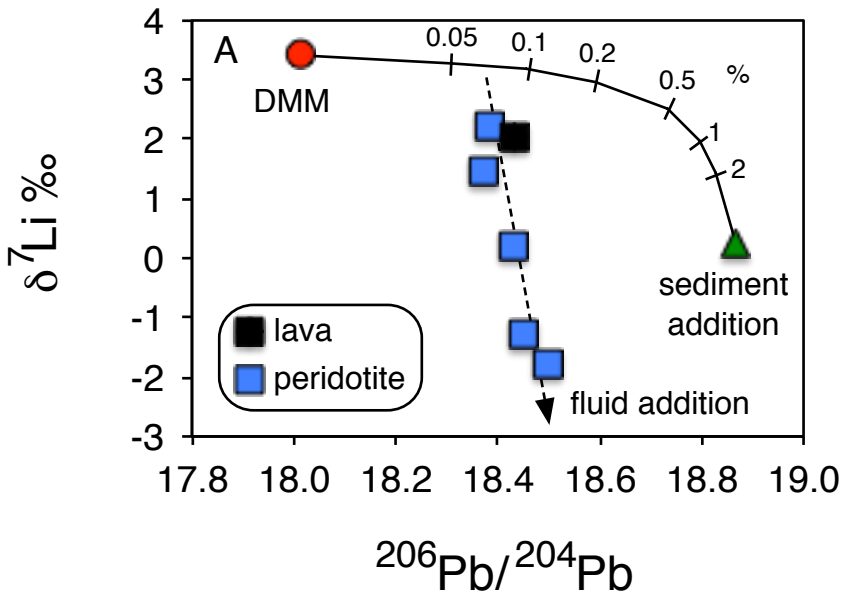
A
DMM
0.05
0.1
0.2
0.5
%
1
2
sediment
addition
lava
peridotite
fluid addition
δ7Li ‰
206Pb/204Pb

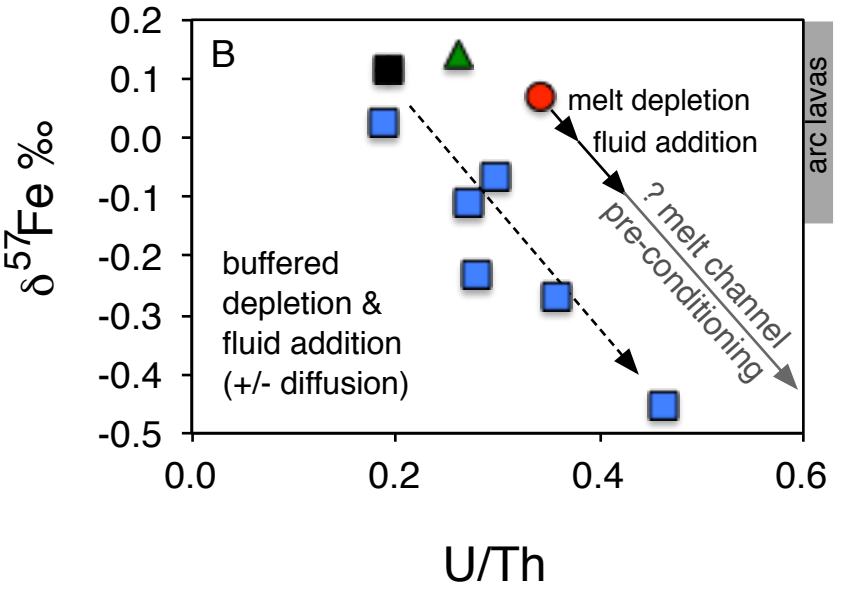
B
melt depletion
fluid addition
? melt channel
pre-conditioning
arc lavas
buffered
depletion &
fluid addition
(+/- diffusion)
δ57Fe ‰
U/Th

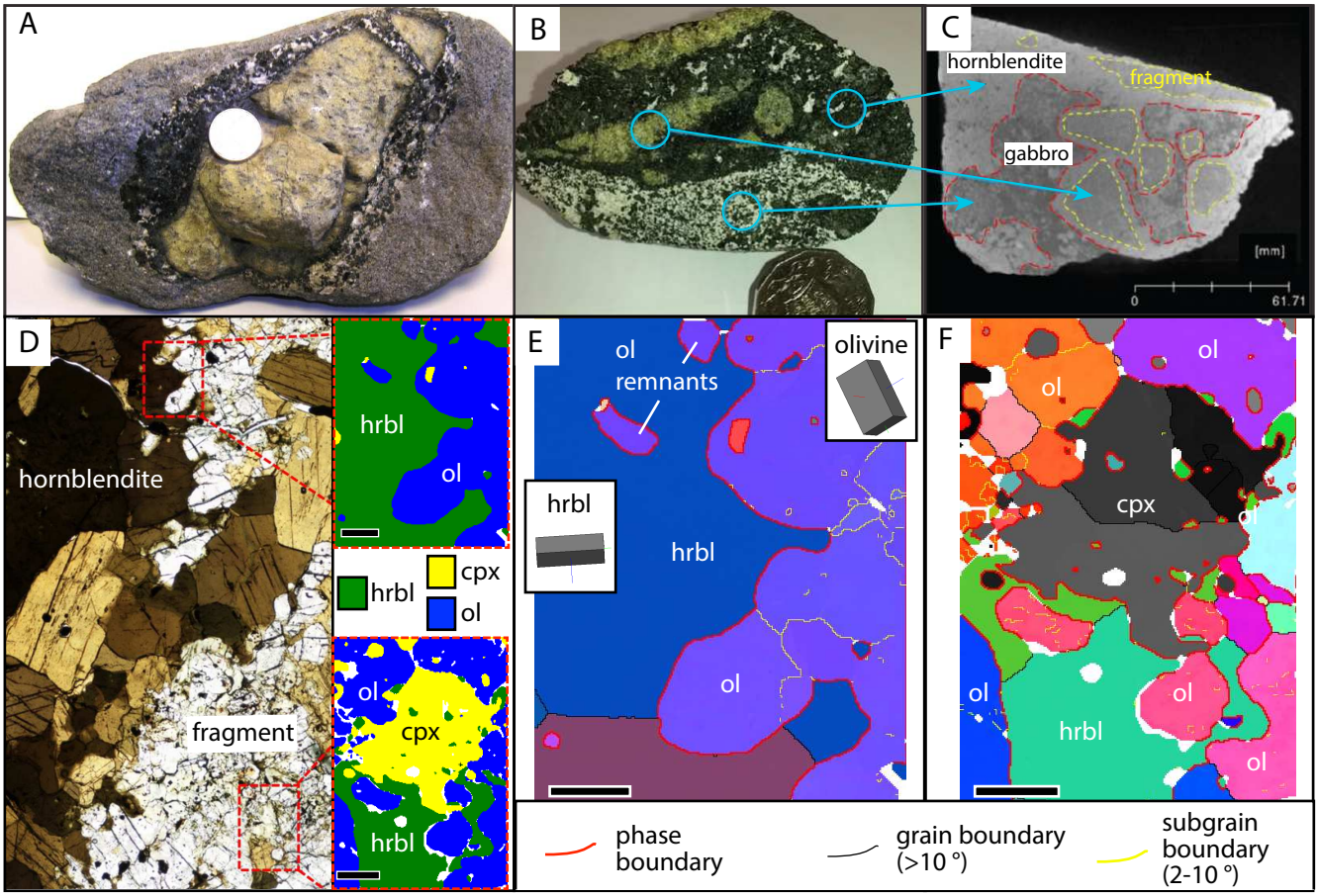
A
B
C
hornblendite
fragment
gabbro
[mm]
0
61.71
D
hornblendite
fragment
hrbl
ol
cpx
hrbl
ol
ol
cpx
hrbl
E
ol
remnants
olivine
hrbl
hrbl
ol
F
ol
ol
cpx
ol
ol
hrbl
ol
phase
boundary
grain boundary
(>10 °)
subgrain
boundary
(2-10 °)

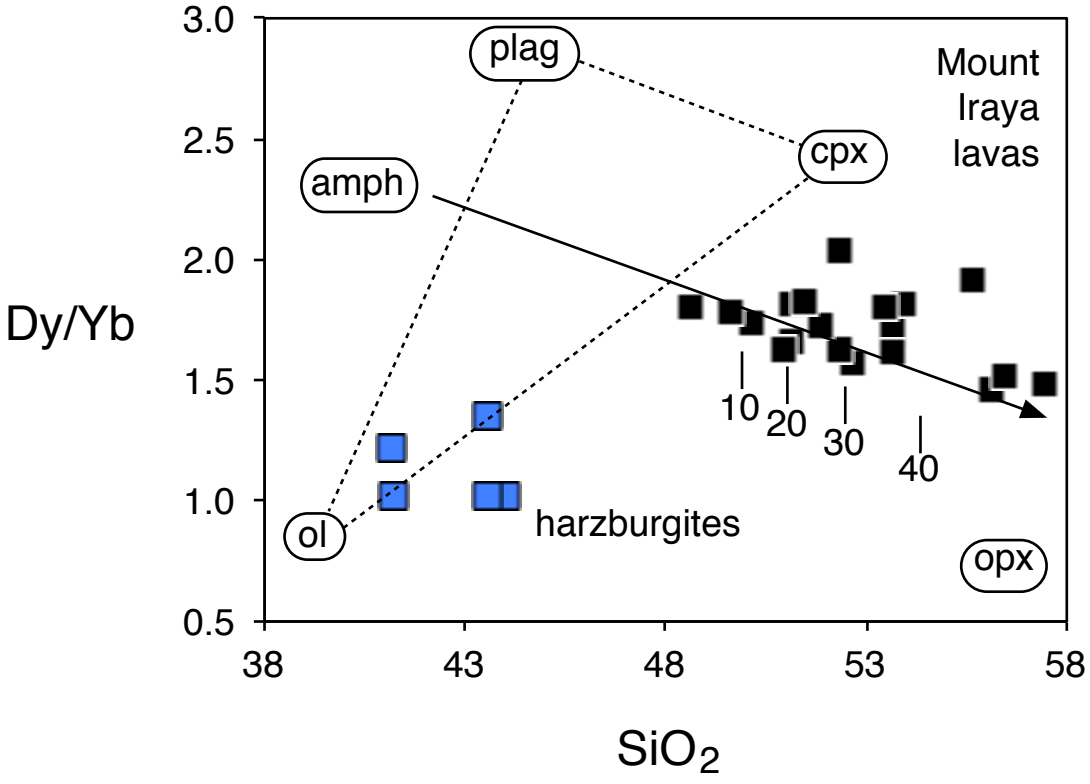
Dy/Yb
3.0
2.5
2.0
1.5
1.0
0.5
38
43
48
53
58
SiO2
plag
cpx
amph
ol
opx
Mount
Iraya
lavas
harzburgites
10
20
30
40

Table DR1. Elemental and isotope compositions of the Batan Island host lava, mantle xenoliths, sediment and unmodified mantle

Sample #	Rock Type	B (ppm)	δ^{11}B ‰	Li (ppm)	δ^{7}Li ‰	FeO*	δ^{57}Fe ‰	Pb (ppm)	^{206}Pb/^{204}Pb	^{207}Pb/^{204}Pb	^{208}Pb/^{204}Pb	^{87}Sr/^{86}Sr
Song 24b	host lava	30.5	-5.65	9.43	2.01	7.03	0.11	13.64	18.435	15.620	38.749	*0.704450*
Song 24b	harzburgite	n/d	n/d	1.77	2.22	8.11	-0.11	0.73	18.384	15.602	38.658	*0.704512*
Song 24a	harzburgite	n/d	n/d	2.29	0.19	10.89	-0.07	0.26	18.431	15.699	38.477	*0.706661*
Song 3a	harzburgite	5.2	n/d	2.65	-1.30	8.69	-0.46	0.49	18.451	15.631	38.724	*0.704685*
Basco 17b	harzburgite	n/d	n/d	1.17	1.42	7.84	-0.27	0.15	18.374	15.628	38.640	*0.704875*
Balu 8	harzburgite	3.2	n/d	2.72	-1.78	7.92	-0.23	0.53	18.496	15.722	38.501	*0.707751*
B103	harzburgite	n/d	n/d	1.38	1.38	8.83	0.03	0.39	n/d	n/d	n/d	*0.704880*
RC17-159	sediment	n/d	-0.5	55.3	0.22	6.97	0.16†	24.20	18.868	15.682	38.276	0.712070
DMM	lherzolite	0.06	-5	0.7	3.4	8.07	0.07	0.023	18.018	15.486	37.903	0.703131

Depleted MORB mantle (DMM) based on Salters and Stracke (2004); Chaussidon and Marty (1995), Stracke et al. (2003); Elliott et al. (2004) and Williams and Bizimis (2014)

*total iron in wt. %; n/d = not determined, †estimated terigenous composition based on MORB

Sr isotope data in italics taken from Turner et al. (2012)

Table DR2. Representative major element analyses of minerals within the xenolith and host lava shown in Fig. 2, plus the groundmass of the lava

Component Component	harzburgite olivine	harzburgite orthopyroxene	harzburgite clinopyroxene	harzburgite Cr-spinel	hornblendite pargasite	gabbro pargasite	gabbro plagioclase	host lava orthopyroxene	host lava clinopyroxene	host lava plagioclase	host lava groundmass
SiO_2 (wt. %)	39.33	56.44	52.18	0.04	40.82	40.53	44.50	54.02	50.39	48.21	58.53
TiO_2	0.00	0.04	0.20	0.00	1.97	2.20	0.00	0.26	0.48	0.00	0.22
Al_2O_3	0.00	1.11	2.49	25.16	13.65	13.52	34.40	1.58	3.79	32.57	20.29
FeO	17.27	11.46	4.33	19.64	5.57	6.27	0.57	17.51	4.53	0.75	4.02
Cr_2O_3	0.02	0.07	0.49	41.71	0.00	0.00	0.00	0.00	0.00	0.00	0.00
Fe_2O_3	0.00	0.00	0.48	0.00	6.18	5.47	0.00	0.20	3.80	0.00	0.00
MnO	0.39	0.38	0.17	0.07	0.14	0.14	0.00	0.48	0.19	0.00	0.12
MgO	43.03	30.28	15.85	13.22	15.11	14.96	0.03	24.92	15.69	0.06	2.32
CaO	0.12	1.18	22.70	0.00	12.38	12.40	19.10	1.89	21.03	16.55	8.37
Na_2O	0.03	0.01	0.26	0.00	2.36	2.14	0.76	0.00	0.22	2.39	4.83
K_2O	0.00	0.00	0.01	0.00	0.97	1.17	0.03	0.00	0.00	0.08	1.15
NiO	0.30	0.05	0.00	0.12	0.00	0.00	0.00	0.00	0.00	0.00	0.00
Total	100.49	101.02	99.16	99.96	99.15	98.80	99.39	100.86	100.12	100.61	99.85

Table DR3. Representative trace element analyses of minerals within the xenolith shown in Fig. 2

Component	harzburgite	harzburgite	harzburgite	hornblendite	gabbro	gabbro
Mineral	olivine	orthopyroxene	clinopyroxene	hornblende	hornblende	plagioclase
Li (ppm)	3.2	1.3	1.67	1.3	1.18	0.48
Be	<0.073	<0.063	0.109	0.412	0.573	0.38
B	<1	5.12	4.75	5.39	3.17	4.42
Sc	7.03	12.09	83.3	100.28	106.18	1.618
V	3	34.25	182.46	500.03	572.27	7.98
Cr	3	1189.47	6616.84	230.16	188.82	<0.99
Co	186	61.09	24.5	50.58	56.02	0.827
Ni	2210	544.43	299.72	303.45	205	1.28
Cu	5.92	1.25	5.14	2.68	2.64	2.69
Zn	157	104.59	26.95	47.61	58.07	5.67
Ga	0.3	2.209	3.61	27.91	26.44	23.44
Rb	0.13	<0.055	0.079	9.44	7.37	3.43
Sr	0.091	0.123	49.81	393.66	362.17	1135.88
Y	0.071	0.824	10.95	17.71	16.92	0.547
Zr	0.17	0.642	18.32	50.47	39.11	4.77
Nb	0.1	<0.0086	0.0219	3.25	2.29	0.322
Cs	0.07	<0.0231	<0.029	0.217	0.028	0.261
Ba	0.5	<0.0178	0.137	253.4	266.26	69.92
La	0.06	<0.0105	2.001	4.63	5.03	2.91
Ce	0.05	0.0304	9.01	17.35	18.28	5.47
Pr	0.05	<0.0041	1.942	3.21	3.13	0.613
Nd	0.32	0.088	12	18.02	16.61	1.88
Sm	0.3	0.053	3.2	4.96	4.42	0.355
Eu	0.09	0.0139	0.738	1.383	1.4	0.286
Gd	0.3	0.094	2.64	4.18	3.76	0.142
Tb	0.04	0.0156	0.354	0.599	0.537	0.0165
Dy	0.3	0.121	2.3	3.74	3.25	0.11
Ho	0.05	0.0408	0.427	0.737	0.704	0.0229
Er	0.2	0.129	1.183	1.817	1.79	0.043
Tm	0.06	0.0283	0.165	0.241	0.229	<0.0093
Yb	0.34	0.161	0.93	1.488	1.479	0.038
Lu	0.06	0.0192	0.133	0.228	0.206	0.0162
Hf	0.17	0.038	1.422	2.098	1.539	0.103
Ta	<0.07	<0.0054	0.0059	0.1402	0.0967	0.0087
Pb	0.21	<0.033	0.12	1.618	1.425	1.465
Th	0.05	<0.0065	0.0789	0.577	0.322	0.53
U	0.05	<0.0058	0.01	0.1093	0.0374	0.112

Table DR4. Re-Os isotope data for olivine from a harzburgite fragment

Re (ppb)	2σ	Os (ppb)	2σ	$^{187}Re/^{188}Os$	2σ	$^{187}Os/^{188}Os$	2σ
0.944	0.014	1.5713	0.0009	22.890	0.144	0.12660	0.0001

GSA Data Repository

Sub-arc xenolith Fe-Li-Pb isotopes and textures tell tales of their journey through the mantle wedge and crust

Simon Turner, Helen Williams, Janne Blichert-Toft, Sandra Piazolo, Mitchel Gerdes, John Adam, Xiao-Ming Liu, Bruce Schaefer and Rene Maury

This data supplement includes Tables DR1-4 in Excel format.

Analytical Methods

Quantitative orientation analysis (Electron back-scatter diffraction) was performed at Macquarie Geoanalytical using the Carl Zeiss IVO SEM at 20kV, high vaccum and 8.0 nA. Patterns were acquired with HKL NordlysNano high sensitivity EBSD detector and indexed using AzTec analysis software (Oxford Instruments). Analyses were acquired on a raster grid with step sizes of 4-10 mm. Post-acquisition analysis was performed using the Channel 5 software (Oxford Instruments) using a "standard" noise reduction (Piazolo et al., 2006). Grain boundaries are defined as areas surrounded by 10º boundaries, while sub-grain boundaries have misorientations less than 10º. Mineral analyses were obtained using a Cameca SX100 with an accelerating voltage of 15 keV and a focused beam current of 20 nA. A defocussed beam was used to measure the groundmass of the host lava. A counting time of 10 seconds was assigned to both peak and background measurements. Spectrometer calibration was achieved using the following standards: Jadeite (Na), Fayalite (Fe), kyanite (Al), olivine (Mg), chromite (Cr), spessartine garnet (Mn), orthoclase (K), wollastonite (Ca, Si) and TiO_2 (Ti). Mineral trace element analyses were performed in situ using a Photon Machines Excite 193 Eximer laser coupled to an Agilent Technologies 7700 Series quadrupole inductively-coupled plasma mass spectrometer, Glitter software and NIST610 Glass as a calbiration standard and BHVO-2G and BCR-2G as reference materials.

The whole rock isotope analyses of the harzburgites reported in Table DR1 were obtained on splits of the same powders used in Turner et al. (2012). Boron isotopic composition was determined at the Istituto di Geoscienze e Georisorse, Pisa, by the dicesium borate method using a VG Isomass 54E positive thermal ionization mass spectrometer, following separation of boron by ion-exchange procedures (Tonorini et al., 1997). Total procedural blanks (8-12 ng) are negligible relative to the amount of sample processed. Correction for isotopic fractionation associated with mass spectrometric analysis was made using a fractionation factor (including correction for ^{17}O

contributions), calculated as $\{(R_{cert}+0.00079)/R_{meas}\}$, relative to NIST SRM 951 ($R_{meas} = {}^{11}B/{}^{10}B_{meas} = 4.0498\pm0.0010$). An aliquot of this standard was processed identically with each batch of samples. Boron isotopic composition is reported in conventional delta notation ($\delta^{11}B$) as per mil (‰) deviation from the accepted composition of NIST SRM-951 ($R_{cert} = 4.04362$). Long-term reproducibility of isotopically homogeneous samples treated with alkaline fusion chemistry is approximately ± 0.5‰ and replicate analyses of all samples agree within this limit. Accuracy was evaluated independently via multiple analyses of the GSJ-JB2 basalt reference standard, for which we obtained an average $\delta^{11}B$ of 7.13 ± 0.19‰ ($2\sigma_{mean}$; n = 17).

Samples (and standards) were prepared for Li isotopic analysis at the University of Maryland by digesting the powders with a 3:1 mixture of concentrated HF and HNO_3 in Savillex® screw top beakers on a hot plate (T~ 90°C). This was followed by addition of HNO_3 and HCl, with drying between each stage of acid addition. The residue was then re-dissolved in 4 M HCl in preparation for four-column ion-exchange chromatography (Rudnick et al., 2004). For each column, 1 ml of cation exchange resin of AG50w-X12, 200-400 mesh (Bio-Rad) was cleaned with HCl and Milli-Q water followed by conditioning, chemical separation and sample collection using an eluent mixture of HCl and ethanol. The first two columns remove major element cations with 2.5M HCl and subsequently 0.15M HCl. The third and fourth columns separate Na from Li with 30% ethanol in 0.5M HCl through a N_2 pressurized ion exchange column (Rudnick et al., 2004). The samples were analyzed for ^6Li and ^7Li on a Nu Plasma multiple-collector inductively coupled plasma mass spectrometer using faraday cups. Li isotopic compositions were analyzed by bracketing the sample, before and after, with the L-SVEC standard. The δ^7Li value ($\delta^7Li = [[{}^7Li/{}^6Li]_{sample} / [{}^7Li/{}^6Li]_{standard} - 1 \times 1000]$) is expressed as per mil deviations from the LSVEC standard. External reproducibility of the isotopic compositions is $\leq \pm1.0$‰ (2σ) based on repeat runs of pure Li standard solutions: in-house standard UMD-1 and international standard reference material IRMM-016.

Iron isotopic analyses followed procedures described in Williams and Bizimis (2014) using a ThermoFisher Neptune multiple-collector inductively coupled plasma mass spectrometer at the University of Durham. Instrumental mass bias was corrected for by sample–standard bracketing where the sample and standard Fe beam intensities (typically 35–40V ^{56}Fe for a standard 10^{11} resistor) were matched to 5%. Mass dependence, long-term reproducibility and accuracy were evaluated by analysis of an in-house FeCl salt standard ($\delta^{57}Fe = -1.06 \pm 0.07$‰; $\delta^{56}Fe = -0.71 \pm 0.06$‰ 2S.D., $n = 35$). The mean Fe isotope compositions of international rock standards BIR-1 (Icelandic basalt) and Nod-PI (Pacific ferromanganese nodule) were: BIR-1, $\delta^{57}Fe = 0.082 \pm 0.01$‰; $\delta^{56}Fe = 0.062 \pm 0.01$‰ (2S.D., $n = 6$), Nod-PI $\delta^{57}Fe = -0.837 \pm 0.02$‰; $\delta^{56}Fe = -0.569 \pm 0.03$‰ (2S.D., $n = 7$). Iron yields were quantitative and chemistry blanks were <0.5ng Fe, negligible compared to the quantities of sample Fe (>300μg) processed.

The Pb isotope compositions were determined on bulk-rock powders by wet chemistry and a Nu Plasma 500 HR multiple-collector inductively coupled plasma mass spectrometer using Tl doping and sample–standard bracketing (Albarede et al., 2004) at the Ecole Normale Supérieure in Lyon. The whole-rock powders were leached in hot 6M HCl, including multiple ultrasonicating steps, prior to attack in a 3:1:0.5 mixture of double-distilled concentrated HF, HNO_3, and $HClO_4$. After fuming with double-distilled concentrated $HClO_4$ to eliminate fluorides from the sample digestion procedure, the samples were taken up in 6M HCl, placed on a hot plate until in complete solution, and evaporated to dryness. Lead was separated by ion-exchange chromatography on 0.5 ml columns filled with Bio-Rad AG1-X8 (100–200 mesh) resin using 1M HBr to elute the sample matrix and 6M HCl to collect the Pb. The total procedural Pb blank was < 20 pg. The NIST 981 Pb standard and the values of Eisele et al. (2003) were used for bracketing the unknowns (every two samples), and added Tl was used to monitor and correct for instrumental mass bias. The external reproducibility, estimated from the repeated NIST 981 measurements, are 100-200 ppm (or 0.01-0.02 %) for ratios based on 204 ($^{206}Pb/^{204}Pb$, $^{207}Pb/^{204}Pb$, $^{208}Pb/^{204}Pb$) and 50 ppm (or 0.005 %) for $^{207}Pb/^{206}Pb$, $^{208}Pb/^{206}Pb$, and $^{207}Pb/^{208}Pb$.

The Re–Os methodology for the analysis in Table DR4 followed techniques described in Bezard et al. (2015). An olivine separate from a harzburgite fragment shown in Fig. 1 was spiked for Re and Os and digested in inverse aqua regia (8 ml 16M HNO_3, 4 ml 12M HCl) by Carius tube dissolution followed by solvent extraction using the methods of Shirey and Walker (1995) and Cohen and Waters (1996). Rhenium was purified following Os extraction using anion exchange chromatography (Lambert et al., 1998) after back extraction in isoamylol. The osmium isotope composition was analysed in negative ion mode on a Thermo-Finnigan Triton at Macquarie University. The Os was loaded onto a Pt filament and analysed using by peak hopping for 200 ratios. Rhenium was determined using a quadrupole Agilent 7500 inductively coupled plasma mass spectrometer. A Re standard solution was analysed to monitor drift and fractionation. The sample was blank-corrected using 1 pg Re and 1.15 pg Os with a $^{187}Os/^{188}Os$ ratio of 0.164. Whole-rock standard (WPR-1; n=3) values in this laboratory average 10.53 ppb Re and 16.66 ppb Os with a $^{187}Os/^{188}Os$ ratio of 0.14466±0.00082, reproducing accepted values (e.g., Cohen and Waters, 1996). Further discussion of standard results and reproducibility is available in Day et al. (2015).

Host-melt – xenolith diffusion

When plotted against the reciprocal of their elemental composition, there is no simple correlation for either δ^7Li or $\delta^{57}Fe$ as would be expected from diffusive interaction between the host magma and xenoliths (Fig. DR1).

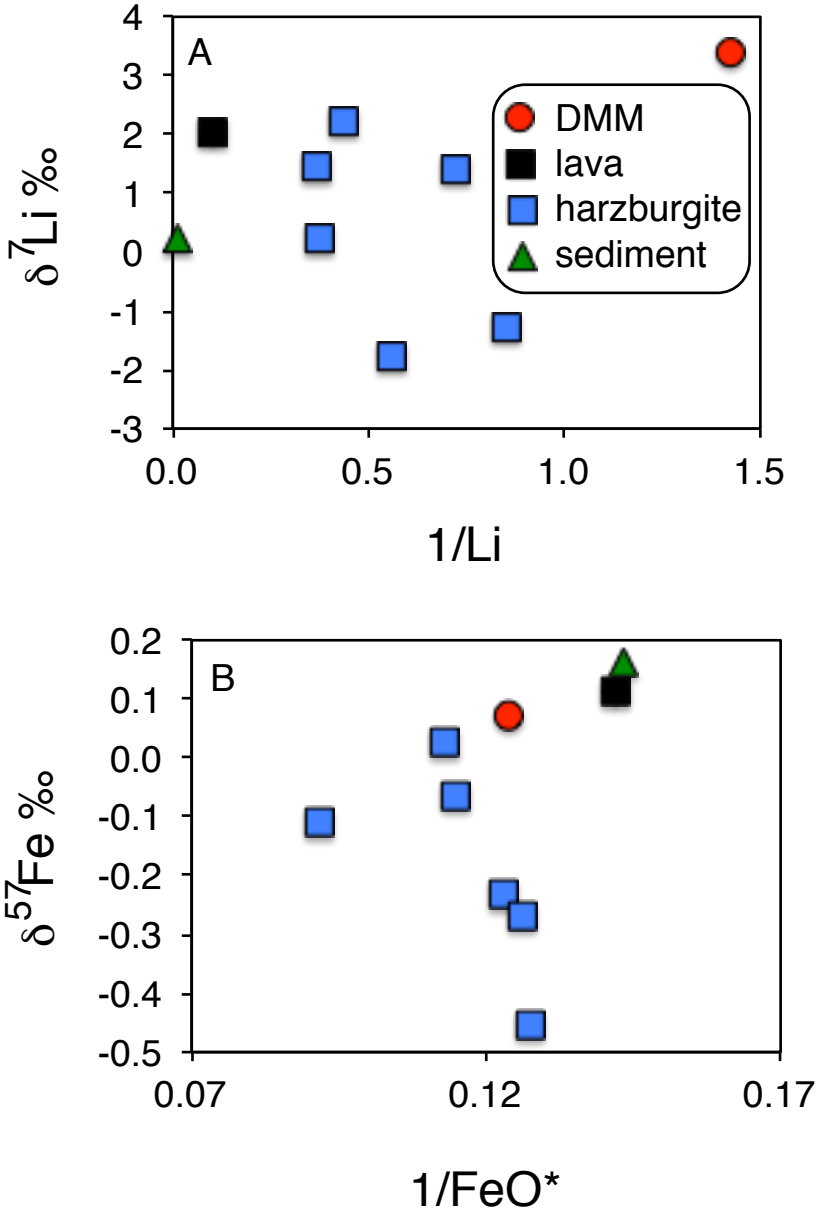

Figure DR1. Isotope – element systematics in Batan xenoliths. A: Plot of δ^7Li versus 1/Li and B: δ^{57}Fe versus 1/FeO* showing that there is no simple correlation as would be expected from diffusive interaction with the mantle wedge or host magma.

Li-Fe isotopic fluid-mantle wedge mixing models

Mixing models between a slab fluid and DMM end-members (δ^{57}Fe = 0.04 ‰; Williams and Bizimis 2016 and references therein) were constructed in order to evaluate if the Fe-Li stable isotope relationships (Fig. DR2) could be explained by the simple addition of an isotopically light fluid to the mantle wedge. In the absence of a direct proxy, the slab fluid component was approximated using Fe and Li concentration and isotopic data for high-temperature hydrothermal fluids vents (Fe isotopes: Rouxel et al., 2008, δ^{57}Fe = -2.67 ‰, [Fe] = 3105 µM; Li isotopes: Chan

et al., 1993 δ^7Li = -6.8 ‰, [Li] = 1421 µM). The slab fluid - mantle wedge mixing model defines a strongly curved line on Fig. DR2, as a result of the extreme contrast in Li/Fe ratios between the fluid and mantle wedge. The contrast between the strong curvature of the mixing line and the broad linear array of the samples serves to demonstrate that simple binary mixing cannot be the dominant process in controlling the Li and Fe isotope systematics of the Batan xenoliths.

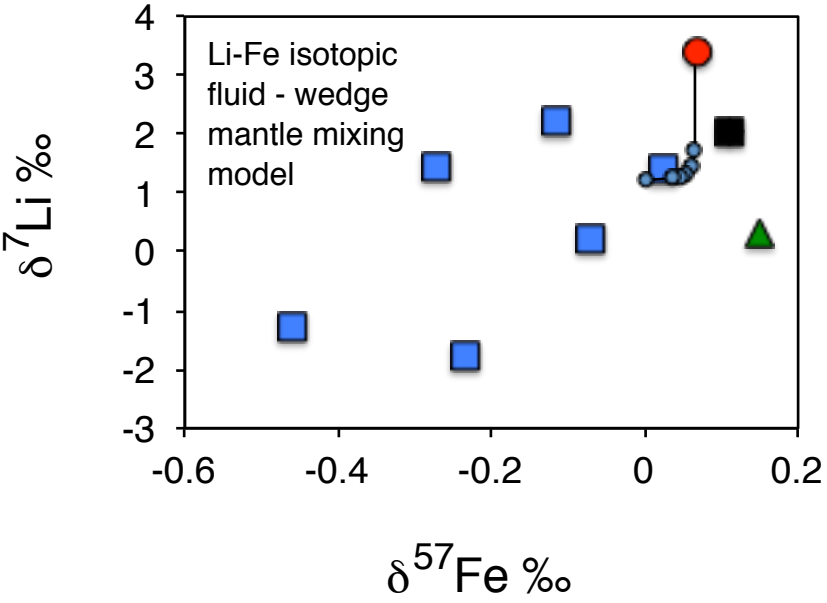

Figure DR2. Plot of δ^7Li versus δ^{57}Fe showing weak positive correlation. Fluid – wedge mixing model is strongly curved relative to the data and cannot reproduce the extent of stable isotope fractionation (marks along curve indicate 10% increments of fluid addition).

References

Albarede, F., Telouk, P., Blichert-Toft, J., Boyet, M., Agranier, A., and Nelson, B.K., 2004, Precise and accurate isotopic measurements using multiple-collector ICPMS: Geochimica et Cosmochimica Acta, v. 68, p. 2725–2744.

Bezard, R., Schaefer, B., Turner, S., Davidson, J.P., and Selby, D., 2015, Lower crustal assimilation in oceanic arcs: insights from an Osmium isotope study of the Lesser Antilles: Geochimica et Cosmochimica Acta, v. 150, p. 330-344.

Chan, L.H., Edmond, J.M., and Thompson, G., 1993, A lithium isotope study of hot springs and metabasalts from mid-ocean ridge hydrothermal systems: Journal of Geophysical Research, v. 98, p. 9653-9659.

Chaussidon, M., and Marty, B., 1995, Primitive boron isotope composition of the mantle. Science, v. 269, p. 383– 386.

Cohen, A.S., and Waters, F.G., 1996, Separation of osmium from geological materials by solvent

extraction for analysis by thermal ionisation mass spectrometry. Analytica Chimica Acta, v. 332, p. 269–275.

Day, J.M.D., Waters, C.L., Schaefer, B.F., Walker, R.J., and Turner, S., 2015, Use of hydrofluoric acid desilicification in the determination of highly siderophile element abundances and Re-Os isotope systematics in mafic-ultramafic rocks: Geostandards and Geoanalytical Research, v. 39, p. 17-30.

Eisele, J., Abouchami, W., Galer, S.J., and Hofmann, A.W., 2003, The 320 kyr Pb isotope evolution of Mauna Kea lavas recorded in the HSDP-2 drill core: Geochemistry, Geophysics, Geosystems, v. 4, doi:10.1029/2002GC000339.

Lambert, D.D., Foster, J.G., Frick, L.R., Hoatson, D.M., Purvis, A.C., 1998, Application of the Re-Os isotopic system to the study of Precambrian magmatic sulfide deposits of Western Australia: Australian Journal of Earth Sciences, v. 45, p. 265–284.

Piazolo, S., Bestmann, M., Spiers, C., and Prior, D.J., 2006, Temperature dependent grain boundary migration mechanisms: Insights from in-situ experiments: Tectonophysics, v. 427, p. 55-71.

Rouxel, O., Shanks, W.C., Bach, W. and Edwards, K.J., 2008, Integrated Fe-and S-isotope study of seafloor hydrothermal vents at East Pacific Rise 9–10 N: Chemical Geology, v. 252, p. 214-227.

Rudnick, R.L., Tomascak, P.B., Heather, B.N., and Gardner, L.R., 2004, Extreme lithium isotopic fractionation during continental weathering revealed in saprolites from South Carolina: Chemical Geology, v. 212, p. 45–57.

Salters, V.J.M., and Stracke, A., 2004, Composition of the depleted mantle: Geochemistry, Geophysics, Geosystems, v. 5, doi:10.1029/2003GC000597.

Shirey, S.B., Walker, R.J., 1998, The Re-Os isotope system in cosmochemistry and high-temperature geochemistry: Annual Review of Earth and Planetary Sciences, v. 26, p. 423-500.

Stracke, A., Bizimis, M., and Salters, V.J.M., 2003, Recycling oceanic crust: quantitative constraints: Geochemistry, Geophysics, Geosystems, v. 4, doi:10.1029/2001GC000223.

Tonarini, S., Pennisi, M., and Leeman, W.P., 1997, Precise boron isotopic analysis of complex silicate (rock) samples using alkali carbonate fusion and ion exchange separation: Chemical Geology, v. 142, p. 129-137.

Turner, S., Caulfield, J., Turner, M., van Keken, P., Maury, R., Sandiford, M., and Prouteau, G., 2012, Recent contribution of sediments and fluids to the mantle's volatile budget: Nature Geoscience, v. 5, p. 50–54.

Williams, H., and Bizimis, M., 2014, Iron isotope tracing of mantle heterogeneity within the source regions of oceanic basalts: Earth and Planetary Science Letters, v. 404, p. 396–407.